

# A mechanically robust transparent coating for anti-icing and self-cleaning applications

Wu, Xinghua; Chen, Zhong

2018

Wu, X., & Chen, Z. (2018). A mechanically robust transparent coating for anti-icing and self-cleaning applications. *Journal of Materials Chemistry A*, 6(33), 16043-16052.  
doi:10.1039/C8TA05692G

<https://hdl.handle.net/10356/81155>

<https://doi.org/10.1039/C8TA05692G>

---

© 2018 The Author(s) . All rights reserved. This paper was published by Royal Society of Chemistry in *Journal of Materials Chemistry A* and is made available with permission of The Author(s).

*Downloaded on 27 Aug 2022 21:24:46 SGT*



## A Mechanically Robust Transparent Coating for Anti-icing and Self-cleaning Applications

Received 00th January 20xx,  
Accepted 00th January 20xx

Xinghua Wu, Zhong Chen\*

DOI: 10.1039/x0xx00000x

[www.rsc.org/](http://www.rsc.org/)

A mechanically robust, transparent coating that displays very low affinity with ice and various liquids is promising for applications in outdoor facilities, marine and aerospace structures. However, such coating is extremely challenging to prepare because some required materials attributes for the diverse functionalities are contradicting to each other. In this work, we demonstrated a sol-gel derived transparent coating with superior performance over the well-studied superhydrophobic coatings in terms of transmittance (~97.8%), ice-adhesion strength, anti-frost accumulation and self-cleaning performance. We have comprehensively investigated the mechanical properties of the transparent solid coating by nano-indentation, pencil scratch, cross-cut adhesion, and dolly pull-off tests according to the respective ASTM / ISO standards. The coating displayed higher hardness and better scratch resistance than the state-of-the-art slippery liquid-infused porous surfaces and polymer coatings. Furthermore, the coating showed good durability after the sand erosion.

### 1. Introduction

Anti-icing coating is a simple and low cost passive method that holds great promise in effectively preventing ice formation and easy ice removal.<sup>1-4</sup> The commonly used evaluation criteria for an anti-icing coating include water repellence, a delay in ice formation either in time or in temperature, and a low ice-adhesion strength no more than 100 kPa.<sup>5,6</sup> Currently, most of the reported anti-icing coatings are not able to satisfy all these criteria. The widely-reported slippery liquid-infused porous surfaces (SLIPS) have been proven to be the most promising way to reduce ice-adhesion strength and increase icing-delay time. SLIPS can achieve a high transparency by choosing the substrate and lubricant liquid with matching refractive indices.<sup>7</sup> However, the key limitations of SLIPS are: i) the infused liquid will be drained away eventually by gravity or capillarity force,<sup>8</sup> and ii) the mechanical property is weak due to the porous structures.<sup>9,10</sup> Another well-discussed anti-icing coating is based on superhydrophobicity. Superhydrophobic coatings have been widely reported for self-cleaning applications, and they also be employed as a candidate for icephobic application since water droplets are able to roll off the coating surface before icing occurs. Superhydrophobic coatings have been fabricated by self-assembly of

nanoparticles or embedding surface modified nanoparticles in sols, polymers, resins or foams.<sup>11-15</sup> Agglomeration of nanoparticles facilitates formation of the necessary hierarchal micro / nanostructures to allow air to be trapped in the structures, leading to decreased water-solid interface and increased water contact angle.<sup>16</sup> However, such superhydrophobic coatings may not always be an advantage for anti-icing applications, as some icing conditions may adversely affect the anti-icing performance. For example, if ice formation is caused by moisture condensation and accumulation, the micro/nanoporous structure will result in a larger (than nominal) contact area between the ice and the substrate. Such contact into the micro / nanoscale pores will increase the ice-substrate contact area and the ice-adhesion strength. In addition, the hierarchal surface structure is mechanically fragile and difficult to maintain under a harsh working condition.<sup>17-20</sup> Moreover, the agglomeration of nanoparticles and the trapped air cause light scattering, reducing the light transmittance of the superhydrophobic coatings. To overcome this problem, researchers found that self-assembly of surface modified with nanoparticles was effective to achieve a high transparency.<sup>21-23</sup> Boal et al. developed a polymer-mediated strategy for the self-assembly of colloidal nanoparticles which can control the agglomeration of nanoparticles.<sup>24</sup> In this regard, Guzman et al. investigated the effect of surface potentials on nanoparticle agglomeration.<sup>25</sup> Hitoshi et al. obtained transparent coatings by trying different types of alcohols used in the suspensions.<sup>26</sup> One major drawback of these coatings is again their poor mechanical property due to the weak structures. Furthermore, increasing the thickness of self-assembled coatings adversely affects the transmittance of coatings with induced porosity.<sup>27, 28</sup> In summary, mechanical properties and transparency are

correspondence to: [aszchen@ntu.edu.sg](mailto:aszchen@ntu.edu.sg)  
School of Materials Science and Engineering, Nanyang Technological University, 50 Nanyang Avenue, 639798, Singapore.

† Electronic Supplementary Information (ESI) available: Surface microstructure of coatings with different sol stirring time; Calculation of visible transmittance of coatings; Mechanisms of detachment of agglomerated nanoparticles; Liquid advancing and receding on the transparent coating; Statistical analysis of icing-temperature of coated and uncoated glass substrate; The measured surface roughness of the transparent coatings before and after sand erosion. See DOI: 10.1039/x0xx00000x

two major limitations for the SLIPS and superhydrophobic coatings due to their porous or rough structures. A new strategy is needed to prepare mechanically robust transparent coatings for icephobic and self-cleaning applications.

## 2 Results and discussion

### 2.1 A smart and low cost strategy to obtain water repellent coatings

Our coating provides: i) a solid, transparent water repellent coating without conventional hierarchical micro / nanostructures; ii) mechanically robust with uniformly distributed nanoparticles through the ceramics-based coating thickness. In addition, we aim to ensure that iii) the preparation method is simple, scalable, and of low cost. To satisfy these requirements, we have prepared a series of coatings derived from a sol-gel system. By varying the stirring time of the sol, the dispersion of nanoparticles in the final coatings changes significantly. To assist uniform dispersion of the nanoparticles, prior surface modification by 1H, 1H, 2H, 2H –perfluorooctyltriethoxysilane (PFOTES) was adopted on half of the added SiO<sub>2</sub> nanoparticles. The surface modified nanoparticles were termed as PFOTES-SiO<sub>2</sub> and used as low surface energy additives. Another half of the SiO<sub>2</sub> nanoparticles were used without any surface treatment to serve as high surface energy nanoparticles. In our experiment, the sol contained tetraethylorthosilicate (TEOS), 3-glycidoxypropyltrimethoxysilane (GLYMO), PFOTES, SiO<sub>2</sub> nanoparticles (10-20 nm), deionized (DI) water and itaconic acid. Transparent glass slides were used as the substrate. To obtain good mechanical properties, the weight percentage of nanoparticles in the final coatings was fixed at 30 wt%.

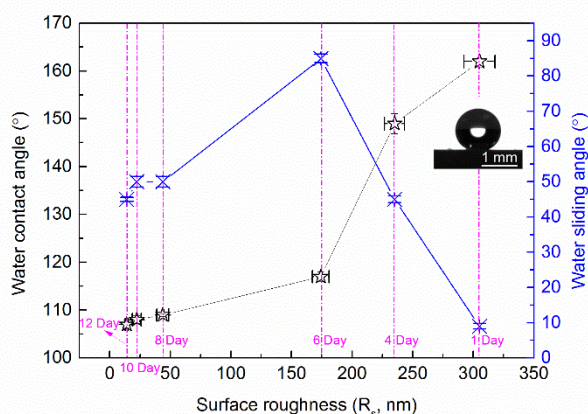


Figure 1 Water contact angles and sliding angles of the prepared coatings at different stirring times versus surface roughness (root-mean-square roughness,  $R_s$ ). Inset shows the water droplet profile on the coating with 1 day's stirring.

Figure 1 presents the effect of surface roughness (root-mean-square roughness,  $R_s$ , Fig. S1) on water wettability. The coating with 1 day's stirring time exhibited superhydrophobicity with a contact angle  $>160^\circ$  (inset in Fig. 1) and a roll-off angle  $<10^\circ$ , owing to the micro /

nanostructures formed by agglomeration of SiO<sub>2</sub> nanoparticles (Fig. S2a and inset). After 4 days' stirring, the size of pores formed on the coating gradually decreased due to the good dispersion of SiO<sub>2</sub> nanoparticles (Fig. S2b), forming new water-solid interfaces with a reduced contact angle. As the stirring time further increased, decreased surface roughness allows water to infuse into the grooves or valleys of coatings, presenting decreased contact angles. Coatings with surface roughness less than 50 nm were obtained with 8 days' stirring or longer. Meanwhile, comparable contact angles  $\sim 110^\circ$  were obtained, and water droplets were in contact with the entire solid surface without trapped air (insets of Fig. S2d-f). To sum up, a clear relationship between surface roughness and the water contact angle can be observed: the water contact angle decreased with decreasing surface roughness. This is consistent with the general understanding that a rougher hydrophobic surface possesses a higher contact angle. In contrast, a distinct difference was observed on the water sliding behavior. The water sliding angle of coatings increased first, and then decreased after 6 days' stirring. This change indicates that the water affinity with the coatings increased with stirring time initially, and then decreased.

Conventionally, a surface is termed as hydrophobic when the water contact angle is larger than  $90^\circ$ . Researchers define a surface superhydrophobic when the contact angle is larger than  $150^\circ$  and roll-off angle is less than  $10^\circ$  following the well-known lotus leaf effect. However, there is another wetting state where the contact angle is larger than  $150^\circ$  but a water droplet does not roll off even when the surface is turned upside down (the rose petal effect).<sup>29-31</sup> The former is a clear indication that water adhesion with the coating surface is very low (repellent), while the latter is high (attractive). Similarly, hydrophobic surfaces with a contact angle  $<150^\circ$  can also display different water affinity. Some researchers termed the hydrophobic repellent state as hydrophobic slippage and attempted to explain the water movement on hydrophobic coatings by the viscosity change of water near the hydrophobic surface and concentration of gas-filled tiny cavities close to it.<sup>32, 33</sup> However, their descriptions also included the superhydrophobic states which rely greatly on the gas-filled tiny cavities. Here, we use the notion of hydrophobic repellent state, to distinguish it from the superhydrophobic state or the hydrophobic attractive state. As described above, a reduced surface roughness allows water to infuse into the grooves or valleys on coating surfaces with 4 and 6 days' stirring (Fig. S2b-c), introducing some degree of mechanical interlocking and capillary forces between water and coating surfaces. Therefore, the coatings presented increased sliding angles. The obtained coatings gradually became flat with further stirring beyond 6 days' stirring. The mechanical interlocking is reduced as the water-solid interface of coatings decreases (Fig. S2d-f). Coatings with 8 days' stirring or longer exhibited comparable water contact angles around  $110^\circ$  and water sliding angle of  $40 \sim 50^\circ$  (Fig. 1), displaying hydrophobic repellent behavior.

### 2.2 Scalable transparency of water repellent coatings and mechanism behind

We take note that existing literatures are mainly focused on increasing the surface roughness to turn hydrophobic coatings to superhydrophobic coatings.<sup>15, 34-37</sup> However, as discussed earlier, increasing the surface roughness by creating rough or porous surfaces would greatly reduce light transmittance of the coatings. In this work, we take a new strategy to resolve the contradicting requirements by reducing the surface

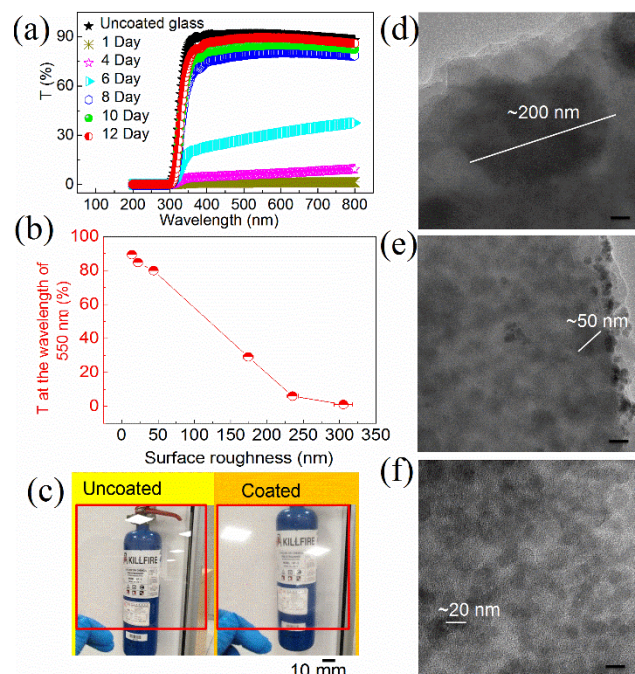


Figure 2 (a) Transmittance of coatings with different stirring times. (b) Relationship between surface roughness and transmittance. (c) Optical transmission of the coating with 12 days' stirring and uncoated glass (size: 10 cm  $\times$  10 cm), and high resolution

roughness of hydrophobic coatings. This has successfully led to a ceramics-based transparent hydrophobic water-repellent coating, which has not been demonstrated before.

Figure 2a displays the transition of a superhydrophobic coating to a hydrophobic repellent coating, accompanied with the change of transmittance of the coatings (Fig. 2b). The corresponding coatings' transmittance relative to glass substrates (Table S1, Supporting information) shows basically the same trend of increased transmittance over decreased surface roughness. The coating (12 days' stirring) exhibited visible-light transmittance as high as 97.8 % (Table S1). This coating, spray-coated on glass substrates (10 cm  $\times$  10 cm), has a uniform transparent layer with a thickness of  $\sim$ 30  $\mu$ m and displays visually comparable transmittance to uncoated glass (Fig. 2c). For comparison, samples with the same amounts of components as the above coatings but without PFOTES were also prepared. The sol without PFOTES needs 14 days' stirring to achieve a transparent coating, and the highest transmittance is around 89.3 % (Fig. S3 and Table S1), which is lower than the transparent hydrophobic coatings with PFOTES (97.8%).

To investigate the reasons behind the transmittance change, we examined the hydrophobic coatings with 6, 10 and 12 days' stirring by TEM (Fig. 2d-f). Stirring time-dependent agglomeration of

nanoparticles is clearly observed. The size of agglomerated nanoparticles in the coating with 6 days' stirring was as large as  $\sim$ 200 nm. With continuously applied shear stress during the stirring, the size of agglomerated nanoparticles gradually decreased to around 50 nm in the coating with 10 days' stirring. Uniform distribution of nanoparticles with the size of 10-20 nm was observed in the coating with 12 days' stirring. The continuous shear action produced by the applied torque of a magnetic stirrer drives the nanoparticles to flow and align in certain direction. This process accelerated the detachment of agglomerated SiO<sub>2</sub> nanoparticles and re-arrangement of the SiO<sub>2</sub> nanoparticles (Fig. S4 and Supporting information). It is well known that the silanol groups on the SiO<sub>2</sub> nanoparticle surface react with PFOTES to impart the hydrophobicity. Thus, the low surface energy PFOTES-SiO<sub>2</sub> nanoparticles serve as spacers and graft to high surface energy SiO<sub>2</sub> nanoparticles through Si-OH groups to reduce the secondary agglomeration. As observed, agglomeration of nanoparticles gives rise to the surface roughness of the coatings. Continuous stirring minimizes the agglomeration size, and at the same time, releases the trapped air. Therefore, the scattering of visible light is eliminated. When the size of agglomerated nanoparticles and air bubbles become smaller than one-tenth of the wavelength of the visible light, the particles will no longer be able to scatter the light,<sup>38</sup> thus a transparent coating is obtained. The size of nanoparticles in the coating after 12 days' stirring was significantly lower than this critical size (1/10 of 400 $\sim$ 700 nm), which explains the high transparency of this coating.

### 2.3 Liquid repellency and self-cleaning properties of THRC

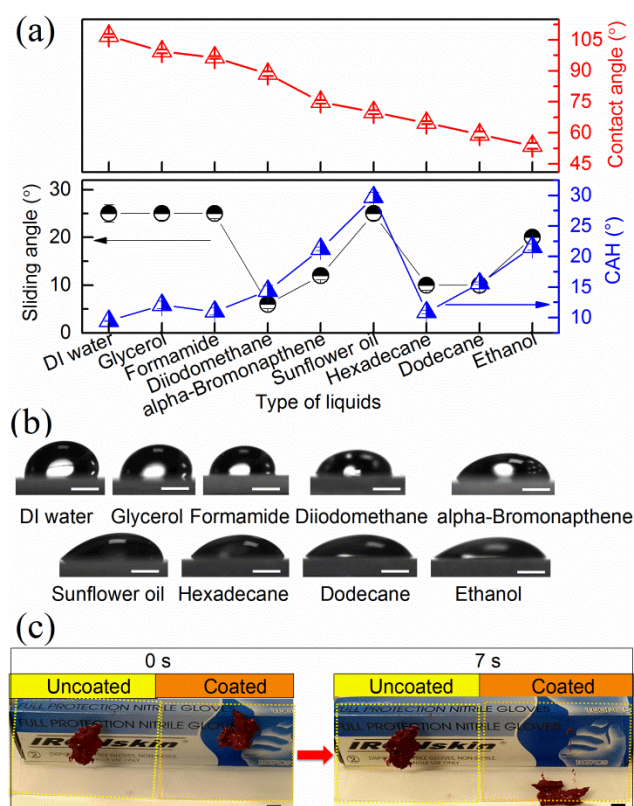


Figure 3(a) Liquid contact angles, sliding angles and CAH on the THRC, and (b) droplet profiles captured during the sliding motion of liquids on the THRC. Scale bar, 1 mm. (c) Captured images of the contaminant movement on THRC coated (right) and uncoated (left). Scale bar, 1 cm.

On the basis of the above findings, we have successfully fabricated a transparent hydrophobic repellent coating (THRC) with 12 days' stirring. The surface roughness and surface energy of the THRC were measured to be  $14.0 \pm 1.2$  nm and  $15.5 \pm 1.0$  mJ/m<sup>2</sup>, respectively. The THRC contains the  $-CF_2$  and  $-CF_3$  groups as shown in the FTIR spectra (Fig. S5), and thus presented low surface energy. The surface energy of the THRC was comparable with 3M<sup>®</sup> Fluorinert<sup>™</sup> and Krytox<sup>®</sup> DuPont<sup>™</sup> liquids that have been used as infused liquids in SLIPS<sup>7,39</sup>

Moreover, the THRC exhibited repellency to liquids with surface energy ranging from 72.8 to 22.1 mJ/m<sup>2</sup> (Fig. 3). We noticed that the overall tendency of the liquid contact angles decreased with decreasing liquid surface energies (Fig. 3a). This is explainable by the classical Young's contact theory. Same phenomenon was also observed on our previously reported superhydrophobic coatings.<sup>15</sup> Besides the static contact angle, we also measured the sliding angles of a 10  $\mu$ l liquid droplet on the THRC surface (Fig. 3a). All the tested liquids exhibited sliding behavior on the THRC with a sliding angle no greater than 25°, indicating reasonably good repellency against these liquids (Video S1). We noticed that the liquid mobility on the coating surface behaved differently with the state-of-the-art SLIPS. SLIPS present no dependence on the surface energy of liquids,<sup>7</sup> the sliding behavior of liquids is due to the interfacial slip of

two immiscible liquids, and the capillary forces are balanced by viscous stresses of the tested liquids. On the contrary, the liquid repellency of the THRC is related to both the low surface energy and the shape of the tested liquids. Generally, a droplet will change shape and become nonaxisymmetric at a tilted angle,  $\alpha$ , resulting in contact angle hysteresis (CAH) which would give rise to a capillary retention force. This force can overcome the gravity, leading to the movement of a droplet. Here, the motion of liquid droplets on THRC greatly depends on the CAH (Fig. 3a) with the exception of DI water, glycerol, and formamide. The difference might be due to their high receding angles (Fig. S6, between 90°~110°) which induce the strong curvature of the free liquid surface counteracting with the viscous force along the direction of liquid motion.<sup>40</sup> As explained by Gao et al.<sup>41</sup>, a droplet may move by sliding at some points of the contact line and rolling at other points or may advance by rolling and recede by sliding. The shape change of a droplet can serve as an activation barrier to movement that is quantified by increasing the liquid-gas interface area. Therefore, the sliding behavior of DI water, glycerol, and formamide is not only determined by the CAH but also the shape of the liquids. Figure 3b shows droplet profiles captured during the sliding motion of liquids. A decrease in curvature at the back of the droplets was observed with decreased surface energy of liquids. This complies with the observed receding angles of the liquids. To verify the self-cleaning effect of the THRC,

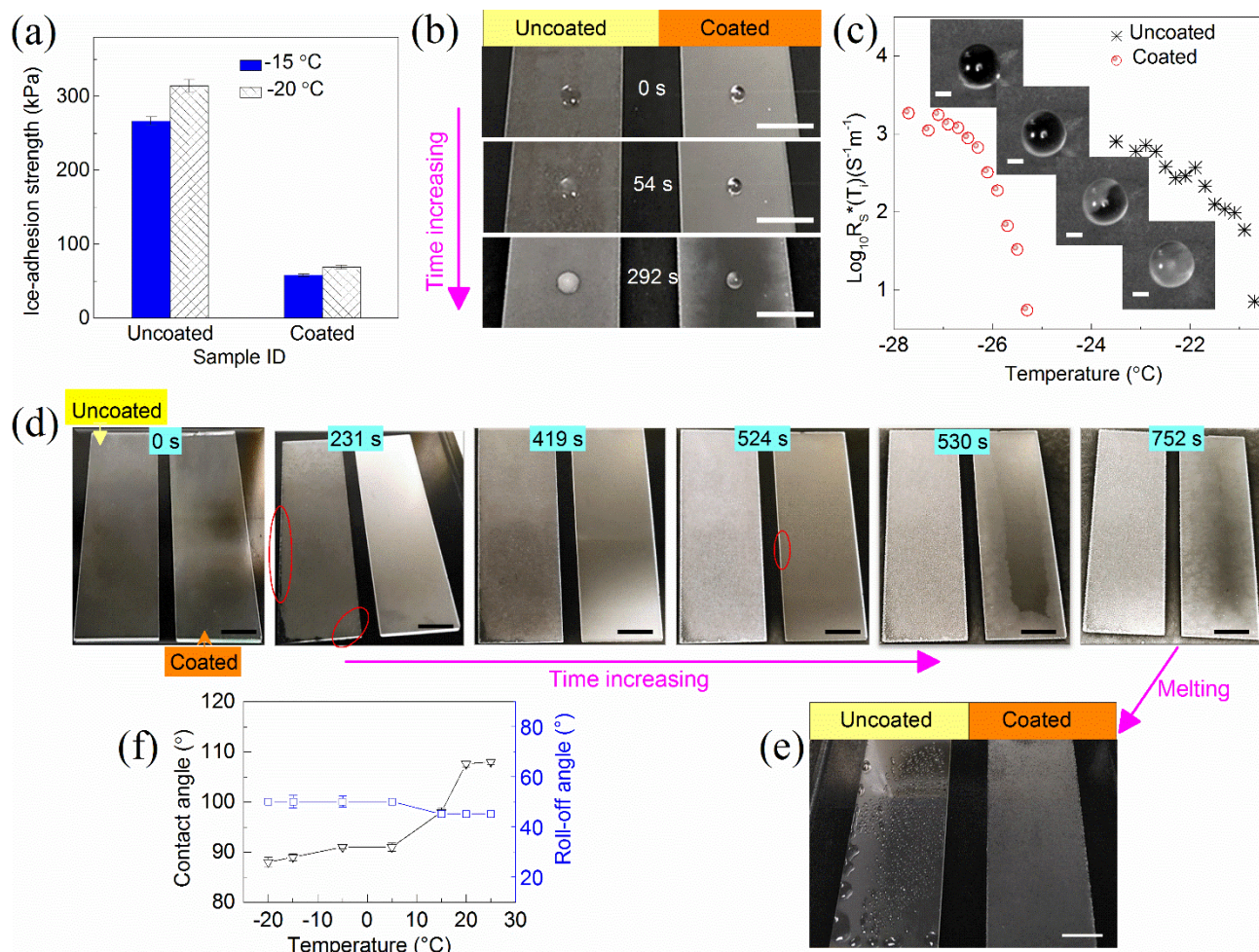


Figure 4 Comparison of (a) ice-adhesion strength, (b) icing-delay time, (c) the calculated line ice-nucleation rate of the THRC coated and uncoated glass, insets are sequential images of the nucleation process on the THRC surface. Scale bar, 1mm. (d) Time-lapse images of frost-formation experiments at -15 °C in still air (80% RH) on the THRC coated and uncoated glass slides, and (e) images of melted ice formed on the THRC coated and uncoated glass slides as shown in (d). Scale bar, 10 mm. (f) Water wettability of THRC under low temperatures (from 25 °C to -20 °C).

contaminant removal tests were carried out on THRC coated and uncoated glass substrate with artificial oily contaminant consisting of acrylic paint, soil and silicone oil. Figure 3c compares the self-cleaning performance of THRC coated glass with uncoated glass. The contaminant easily slid down the THRC in 7 s with only a small amount of residue, demonstrating the self-cleaning ability of THRC. On the other hand, the contaminant stayed firmly on an uncoated glass.

#### 2.4 Robust anti-icing properties of THRC

In addition to high transparency and self-cleanliness, the THRC exhibited ice-adhesion strength as low as  $58.2 \pm 1.5$  kPa and  $69.5 \pm 2.1$  kPa at  $-15$  °C and  $-20$  °C, respectively (Fig. 4a). The THRC coating has a reduced ice-adhesion strength to less than 1/3 of the uncoated one ( $266.8 \pm 5.2$  kPa and  $314.3 \pm 8.7$  kPa at  $-15$  °C and  $-20$  °C, respectively) and the transparent coating without PFOTES ( $208 \pm 4.6$  kPa and  $255 \pm 7.3$  kPa at  $-15$  °C and  $-20$  °C, respectively, Fig. S7a). This is as expected since the uncoated glass and the transparent coating without PFOTES presented hydrophilic properties (Fig. S7b), having a stronger interaction with water molecules. The icing-delay time of the THRC coated and uncoated glass is compared in Fig. 4b. The droplet on the uncoated glass slide (Fig. 4b left) started to freeze after  $54.0 \pm 2.6$  s, whereas the THRC coated one (Fig. 4b right) started icing after  $292 \pm 4.1$  s (delayed 238 s compared with that of an uncoated glass slide) (Video S2, note that the time starts count only after the substrate surface temperature has reached the pre-set temperature of  $-15$  °C).

To comprehensively study the ice nucleation behaviors of the THRC coated and uncoated glass, 500 cycles of icing and deicing events were recorded and statistically analysed. The mean icing temperature of the THRC glass was  $\sim 5$  °C lower than the uncoated ones (Fig. S8 and Table S2 in Supporting information). Regarding the hot debate about the initiation site of nucleation, we observed directly that ice nucleation initiated at the three-phase contact line on the THRC coated and uncoated glass with the help of a high-speed camera system (Video S3), which is in agreement with some recent reports.<sup>42-45</sup> Insets in Fig. 4c show the sequential images of the nucleation process on the THRC surface. Further investigation of the statistical nucleation rate on the three-phase contact line based on Fig. S8 and Table S3 in Supporting information verified the low nucleation rate of the THRC coated glass (Fig. 4c). For any given temperature in the range, the nucleation rate for the THRC coated glass is always much lower than the uncoated glass, which perfectly explains the lower icing temperature.

To understand the frost formation behavior on the THRC coated glass at freezing conditions, samples were placed on a cooling stage without water droplets (Video S4). Water vapor was first cooled down to fog up the sample surface and then visible water droplets were formed. The dew drops started to freeze when the temperature is cooled below the freezing point. Figure 4d compares the resistance to frost formation of the THRC glass in comparison with the uncoated one at  $-15$  °C and 80 % relative humidity (RH). It was observed that the icing of dew droplets on the bottom of the uncoated glass (circled region on the left hand side sample) took place after  $231 \pm 2.0$  s. At  $419 \pm 2.4$  s, the whole uncoated glass surface was covered with ice. While icing started from the uncoated edge of the THRC coated glass at  $524 \pm 3.9$  s (circled region on the right hand side sample), and then ice gradually spread to the center

of the surface until full coverage at  $752 \pm 4.5$  s. The THRC coated glass presented significant delay in frost formation.

A significant resistance to water condensation of the THRC coated glass slide was observed during the melting cycles of the frost-formation experiment. When being heated from  $-15$  to  $25$  °C at  $10$  °C/min, the THRC coated glass slide demonstrated better repellence against water condensation as shown in Fig. 4e. Tiny water mists were observed on the coated glass. In contrast, large and continuous water droplets were formed on the uncoated glass. Besides, the water contact angles and sliding angles of THRC at low temperatures also verified its good resistance to water condensation (Fig. 4f). A decrease in the water contact angle of THRC were observed when the temperature was reduced from  $25$  °C to  $-20$  °C due to the condensation effect. However, it is noteworthy that the contact angle of all the tested coatings approached a steady-state value of around  $90^\circ$  when the temperature falls below zero degree. Moreover, a  $10$   $\mu$ l water droplet could slide down the THRC even when the temperature was  $-20$  °C, and there was only a slight increase in the sliding angle at different temperatures, indicating a reasonably good condensation resistance of THRC. The water repellent nature of the THRC helps protect the surface from incoming moisture / water and also ensure low ice adhesion, making it capable of delaying ice formation and easily removing formed ice.

#### 2.5 Mechanical robustness and durability of THRC

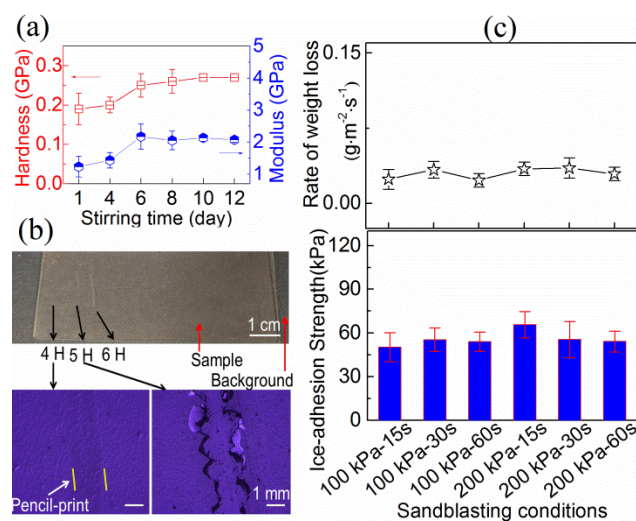


Figure 5 (a) The hardness and modulus of coatings with different stirring time measured by nanoindentation, (b) the measured pencil-scratch resistance of the THRC and microscope images of the scratched area, and (c) rate of weight loss of the THRC under different sandblasting conditions, and the corresponding ice-adhesion strength of coatings after sandblasting.

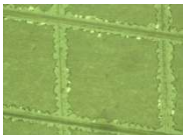

The THRC layer, comprising ceramic sol and a high weight percentage of nanoparticles, possess a much higher hardness compared to superhydrophobic coatings and polymer-based water repellent coatings. An increase in stirring time has significantly increased the hardness and modulus of our coatings (Fig. 5a). This is reasonable due to the gradually reduced porosity of our coatings. The THRC presented the highest hardness and modulus of  $270 \pm 10$  MPa and  $2.07 \pm 0.08$  GPa, respectively. Although the modulus and hardness is lower than that of iCVD film,<sup>46</sup> they are comparable to

the aeronautical livery coating<sup>47</sup> as shown in Table 1. In addition, other mechanical properties such as pencil scratch test, cross-cut adhesion and pull-off adhesion were carried out on the THRC to further investigate the extent of coating adhesion to the substrate surface. The pencil hardness was 4 H according to ASTM D3363 standard test method as shown in Fig. 5b. The 4 H pencil scratch resistance of the THRC coating is higher than available reports (Table 1).<sup>48-50</sup> The coating also exhibited good adhesion to substrates: the cross-cut adhesion of 5 B (based on ASTM D 3359) was obtained for the coating on epoxy substrates and 4 B on glass substrates. The results are comparable to the recently published anti-icing coatings (Table 1).<sup>47, 50-53</sup> A dolly pull-off adhesion strength of  $5.12 \pm 0.07$  MPa was obtained according to ISO 4624 standard test method. The adhesion strength is more than two times higher than that of the aeronautical livery coating<sup>47</sup> and the silicone

elastomer coating (Table 1).<sup>54</sup> Comprehensive mechanical studies have verified the superior mechanical properties of the THRC to the state-of-the-art superhydrophobic coatings, SLIPS and polymer coatings.

To study the mechanical durability of anti-icing coatings, researches employed eraser rubbing,<sup>55</sup> sandpaper abrasion,<sup>56</sup> and sand erosion tests.<sup>57</sup> In this study, sand erosion test was carried out (size of sands: 10 ~ 40  $\mu\text{m}$ ; pressure: 100 kPa and 200 kPa) to investigate the durability of the THRC. As shown in Fig. 5c, the rate of weight loss is approximately  $0.025 \text{ g}/(\text{s}\cdot\text{m}^2)$  under the applied pressures. Although the sandblasting test has slightly roughened the surface (Fig. S9), the THRC could still maintain a low ice-adhesion strength in the range 50-60 kPa at  $-20^\circ\text{C}$ , indicating its robust icephobicity under sand erosion environment.

Table 1 The hardness, modulus, scratch resistance and adhesion strength to the substrates of the THRC in comparison with other available reports.

	Nanoindentation		Cross-cut adhesion		PosiTest Pull-Off adhesion test (MPa)	Pencil scratch resistant
	Hardness (MPa)	Modulus (GPa)	On glass slide	On GFRE		
THRC	270 $\pm$ 10	2.07 $\pm$ 0.08	 4 B (5 % delaminated areas due to scratch)	 5 B (No delamination, smooth cut)	5.12 $\pm$ 0.07 (on GFRE)	4H
Bilayer icephobic film synthesized on steels or silicon wafers via iCVD <sup>46</sup>	479 $\pm$ 7	19.1 $\pm$ 1.2	N/A		N/A	N/A
Aeronautical livery coating on the carbon fiber reinforced polymer (CFRP) <sup>47</sup>	141 $\pm$ 9	4.8 $\pm$ 0.3	5 B on the CFRP		2.41 $\pm$ 0.04 (on CFRP)	N/A
An Icephobic paint <sup>48</sup>	N/A	N/A	N/A		N/A	2 H
A hybrid film (weight ratio: SiO <sub>2</sub> (sol)/copolymers=0.8) <sup>49</sup>	N/A	N/A	0 B on glass and Al substrates		N/A	4 B
Ice Release Coating <sup>50s</sup>	N/A	N/A	5B on aerospace exterior coatings		N/A	2H~3H
Al <sub>2</sub> O <sub>3</sub> /PTFE icephobic coatings <sup>51</sup>	N/A	N/A	5 B of PTFE on the anodized Al 6061		N/A	N/A
An icephobic superhydrophobic coating <sup>52</sup>	N/A	N/A	5 B on aluminium alloys		N/A	N/A
Icephobic hierarchically textured coatings <sup>53</sup>	N/A	N/A	5 B on aluminium surfaces		N/A	N/A
Silicone elastomer coatings <sup>54</sup>	Without silane-based intermedia layer	N/A	N/A		0.431	N/A
	With silane-based intermedia layer	N/A	N/A		1.494	N/A

### 3. Conclusions

We have demonstrated a simple method to prepare a mechanically robust, transparent, icephobic coating with self-cleaning property. We prove that sol-gel coatings with large percentage of nanoparticles could achieve a high level of transparency once the particles are well dispersed through stirring in the sol preparation stage. Benefited from this method, large-scale transparent icephobic coatings with good resistance to water condensation have been fabricated. Furthermore, the transparent, ice/liquids repellent coating demonstrates high hardness, scratch resistance and good adhesion to the substrates. The sol-gel method is simple, low cost, and applicable to complex shapes and large structures. Therefore, our coating holds great promise for practical anti-icing and self-cleaning applications.

### Experimental

#### Materials

Tetraethylorthosilicate (TEOS), 3-glycidoxypropyltrimethoxysilane (GLYMO), 1H, 1H, 2H, 2H-perfluorooctyltriethoxysilane (PFOTES), SiO<sub>2</sub> nanoparticles with particle size around 10-20 nm, and itaconic acid were obtained from Sigma-Aldrich. Methanol (99%) was obtained from Fisher Scientific. Glycerol, formamide, diiodomethane, *a*-bromonaphthalene, sunflower oil, hexadecane, dodecane and ethanol used for contact angle tests and silicone oil for self-cleaning test were obtained from Sigma-Aldrich. Acrylic paint was purchased from Tang Art, China. Microscope glass slides (25.4 mm × 76.2 mm) and cover glass (Diameter: 22 mm and thickness 0.13~0.16 mm, used for ice-nucleation temperature tests) were obtained from Sailboat Lab Co., Ltd. and Marienfeld, respectively. Glass fiber reinforced epoxy (GFRE) substrates used for PosiTest Pull-Off adhesion test were purchased from Thailand. Glass substrates with size of 10 cm × 10 cm × 1.1 mm (BBL-001) used for scalability demonstration were purchased from Zhuhai Kaivo Optoelectronic Technology Co., Ltd., China.

#### Methods

##### 1. PFOTES-SiO<sub>2</sub> nanoparticles Preparation

0.5 ml PFOTES was hydrolyzed in 48ml methanol with 1.5ml water for 24 h and diluted in methanol with volume ratio of 1:2. After that, 0.75 g SiO<sub>2</sub> nanoparticles were added to the diluted PFOTES solution at room temperature. The mixture was first placed in an ultrasonic bath for 30 min, and then magnetically stirred at speed of 500rpm for 24 h. After stirring, the mixture was centrifuged at 2000 rpm for 5 min. The obtained hydrophobic silica was subsequently denoted as PFOTES-SiO<sub>2</sub>. The above-prepared PFOTES-SiO<sub>2</sub> nanoparticles were used as low surface energy fillers. The original SiO<sub>2</sub> nanoparticles obtained from Sigma-Aldrich were used as high surface energy fillers.

##### 2. Sol-Gel Preparation

The sol matrix was prepared using 20 ml methanol, mixed with 5 ml 1 wt. % PFOTES solution, 0.004 mol TEOS, 0.02 mol GLYMO and 0.076 mol deionized (DI) water. The mixture was magnetically stirred for 2 h. The prepared PFOTES-SiO<sub>2</sub> and 0.75 g SiO<sub>2</sub>

nanoparticles were added to the sol matrix and placed in an ultrasonic bath for 15 min, and then placed under a magnetic stirrer at speed of 500rpm for 1 day, 4 days, 6 days, 8 days, 10 days, and 12 days. **In comparison, samples without PFOTES but with same amount of other components were also prepared and stirred for up to 16 days.** The obtained sols were spray-coated onto the glass slides and GFRE substrates, separately, through an airbrush kit (AS06KB) with a 1.5 mm diameter nozzle using compressed air (with pressure at 345 kPa). The distance between the airbrush and the substrate was kept at 8 cm. Finally, the prepared samples were cured in an oven at 110 °C for 1.5 h.

#### Characterization

The surface morphology of the coatings was scanned using a field emission scanning electron microscope (FESEM, JSM-6360, Japan). Atomic force microscopy (AFM, Asylum Research Cypher S, U.S.A.) was used for imaging surface topology of the coatings. The surface roughness was also obtained from the AFM measurement. The reported roughness data are the average of at least three measurements obtained at different locations of the coatings. The scanned area is 5 μm × 5 μm. Transmission electron microscopy (TEM, JEOL 2100 HR, Japan) operating at 200 kV was used to observe the distribution of nanoparticles in the coatings. The transmittance of the coatings was examined by UV-VIS spectrophotometer (Shimadzu UV-2501PC, Japan). **FTIR spectra of the coatings were obtained using a Frontier™ IR/FIR spectrometer (Perkin-Elmer Inc.). The tested tablet sample was prepared by mixing the coating fragments, scrapped from the coatings, and standard KBr powders with weight ratio of 1:20, followed by compression.**

The contact angles, sliding angles, receding angles and advancing angles of liquids were measured with a contact angle system (OCA 20, Dataphysics Co., Germany). The water wettability of coatings under low temperature was measured on the cooling stage of Dataphysics OCA 20 system. The temperature was set at 25, 15, 5, -5, -15, and -20 °C. Measurement was carried out when the temperature of samples reached the targeted temperature. The surface energy of coatings was measured according to the Owens, Wendt, Rabel and Kalble (OWRK)<sup>58-60</sup> method, in which water and ethanol were used as polar liquids, while diiodomethane was used as a non-polar liquid.

To investigate the contaminant-removal performance of the coatings, artificial oil contaminant was prepared by blending acrylic paint, soil and silicone oil with weight ratio of 1:1:1.3. Before applying the contaminant, the samples were tilt at an angle of 60° to the horizontal plane.

Measurements of ice-adhesion strength between an ice block and coating surfaces followed the scheme from our group's previous report<sup>36</sup>. A Teflon mold with an inner diameter of 18 mm was filled with DI water, and then covered with a coated substrate on top. The whole set was placed upside down in a climate chamber (Cincinnati Sub-Zero environmental chambers, USA) for 24 hours at -15 °C and -20 °C, respectively.

To investigate the icing-delay effect, our transparent hydrophobic repellent coating (THRC) and uncoated glass slides were directly placed on the cooling stage of Dataphysics OCA 20



system first. A 10  $\mu\text{L}$  water droplet was placed on the test surfaces, and then the temperature was decreased from room temperature to  $-15\text{ }^\circ\text{C}$ . The ramp rate was set as  $5\text{ }^\circ\text{C}/\text{min}$ . The time at which the droplet started to freeze was recorded as icing-delay time. Besides, the ice-nucleation process of the water droplets was recorded by a high speed camera (Phantom Micro 120). The melting process of the frozen droplets was also captured by the built-in camera of Dataphysics OCA 20 system with a ramp rate of  $10\text{ }^\circ\text{C}/\text{min}$ .

The ice-nucleation temperature of coatings was studied by our group's previously reported self-designed automatic measurement system<sup>45</sup>. A 10  $\mu\text{L}$  DI water droplet was placed on the center of a sample surface, and the test chamber was cooled from ambient temperature down to a set low temperature at  $-30\text{ }^\circ\text{C}$ . The ramp rate from ambient temperature to  $0\text{ }^\circ\text{C}$  was set at  $40\text{ }^\circ\text{C}/\text{min}$ , while the ramp rate from  $0\text{ }^\circ\text{C}$  to  $-30\text{ }^\circ\text{C}$  was set as  $5\text{ }^\circ\text{C}/\text{min}$ . The cooling stops once the droplet was frozen and the freezing temperature was recorded. After which, the iced droplet was heated up to ambient temperature and held for 2 min to ensure a complete melting of the ice before the next cycle began. Icing temperatures of 500 cycles for each water droplet were recorded and statistically analyzed.

The elastic modulus and hardness of the deposited coatings were investigated using a nano-indenter (Nano-Indentation & Micro-Scratch System, Wrexham, United Kingdom) with indentation depth of 1800 nm. For each sample, 15 points (in 3 lines, 5 points each line) were tested. Pencil scratch test of the coatings was assessed using a commercial pencil scratch tester (Scratch Hardness Tester Model 291, ERICHSEN) according to ASTM D3363 Standard Test Method. The coating adhesion on glass slides and GFRE substrates was assessed by cross-cut tape adhesion test based on ASTM D3359 Standard Test Method. After pencil-scratch and cross-cutting, the coatings were examined under an optical microscope (Olympus BX51). The adhesion strength test was conducted by PosiTest Pull-Off adhesion test according to ISO 4624 Standard Test Method. Aluminum dollies with diameter of 20 mm were used to apply the pull-off load.

To study the durability of the coatings, the coatings were eroded by sand using a micro-sand blaster (Comco Inc.). The size of silica ( $\text{SiO}_2$ ) sand particles ranges from 10  $\mu\text{m}$  to 40  $\mu\text{m}$ . The distance between the blaster nozzle and a sample surface was kept at 15 cm. The pressure was set as 100 kPa and 200 kPa, and the erosion time lasted for 15 s, 30 s, and 60 s. The eroded area on the samples was fixed at  $1.13\text{ cm}^2$  (corresponding to a circle 1.5 cm in diameter). The weight loss of eroded coatings was recorded under the different erosion conditions. After the sand erosion, the roughness of the eroded surfaces was measured by a surface profiler (Alpha-Step IQ Surface Profiler, Kla Tencor, USA) with a scan length of 5 mm. The ice-adhesion strength after the sand erosion was also recorded at  $-20\text{ }^\circ\text{C}$ .

## Conflicts of interest

There are no conflicts to declare.

## Acknowledgements

Financial support from Nanyang Technological University in form of a research scholarship, and the Agency for Science, Technology and Research (A\*STAR) of Singapore (SERC 1528000048) is gratefully acknowledged.

## Notes and references

- 1 L. Bocquet and E. Lauga, *Nat. Mater.*, 2011, **10**, 334-337.
- 2 P. Guo, Y. Zheng, M. Wen, C. Song, Y. Lin and L. Jiang, *Adv. Mater.*, 2012, **24**, 2642-2648.
- 3 M. J. Kreder, J. Alvarenga, P. Kim and J. Aizenberg, *Nature Reviews Materials*, 2016, **1**, 15003.
- 4 Y. Shen, H. Tao, S. Chen, L. Zhu, T. Wang and J. Tao, *RSC Adv.*, 2015, **5**, 1666-1672.
- 5 K. Golovin, S. P. Kobaku, D. H. Lee, E. T. DiLoreto, J. M. Mabry and A. Tuteja, *Sci. Adv.*, 2016, **2**, e1501496.
- 6 V. Hejazi, K. Sobolev and M. Nosonovsky, *Sci. Rep.*, 2013, **3**, 2194.
- 7 T. S. Wong, S. H. Kang, S. K. Tang, E. J. Smythe, B. D. Hatton, A. Grinthal and J. Aizenberg, *Nature*, 2011, **477**, 443-447.
- 8 J. Chen, R. Dou, D. Cui, Q. Zhang, Y. Zhang, F. Xu, X. Zhou, J. Wang, Y. Song and L. Jiang, *ACS Appl. Mater. Interfaces*, 2013, **5**, 4026-4030.
- 9 R. Xiao, N. Miljkovic, R. Enright and E. N. Wang, *Sci. Rep.*, 2013, **3**.
- 10 J. D. Smith, R. Dhiman, S. Anand, E. Reza-Garduno, R. E. Cohen, G. H. McKinley and K. K. Varanasi, *Soft Matter*, 2013, **9**, 1772-1780.
- 11 B. P. Binks and T. S. Horozov, *Angew. Chem.*, 2005, **117**, 3788-3791.
- 12 R. G. Karunakaran, C. H. Lu, Z. Zhang and S. Yang, *Langmuir*, 2011, **27**, 4594-4602.
- 13 H. Zhou, H. Wang, H. Niu, A. Gestos, X. Wang and T. Lin, *Adv. Mater.*, 2012, **24**, 2409-2412.
- 14 S. G. Lee, D. S. Ham, D. Y. Lee, H. Bong and K. Cho, *Langmuir*, 2013, **29**, 15051-15057.
- 15 X. Wu, Q. Fu, D. Kumar, J. W. C. Ho, P. Kanhere, H. Zhou and Z. Chen, *Mater. Des.*, 2016, **89**, 1302-1309.
- 16 A. B. D. Cassie and S. Baxter, *J. Chem. Soc. Faraday Trans.*, 1944, **40**, 0546-0550.
- 17 T. Furuta, M. Sakai, T. Isobe and A. Nakajima, *Langmuir*, 2010, **26**, 13305-13309.
- 18 R. Karmouch and G. G. Ross, *J. Phys. Chem. C*, 2010, **114**, 4063-4066.
- 19 L. Yin, Q. Xia, J. Xue, S. Yang, Q. Wang and Q. Chen, *Appl. Surf. Sci.*, 2010, **256**, 6764-6769.
- 20 T. Verho, C. Bower, P. Andrew, S. Franssila, O. Ikkala and R. H. Ras, *Adv. Mater.*, 2011, **23**, 673-678.
- 21 J. Bravo, L. Zhai, Z. Wu, R. E. Cohen and M. F. Rubner, *Langmuir*, 2007, **23**, 7293-7298.
- 22 M. Layani and S. Magdassi, *J. Mater. Chem.*, 2011, **21**, 15378-15382.
- 23 Y. Rahmawan, L. Xu and S. Yang, *J. Mater. Chem. A*, 2013, **1**, 2955-2969.

- 24 A. K. Boal, F. Ilhan, J. E. DeRouchey, T. Thurn-Albrecht, T. P. Russell and V. M. Rotello, *Nature*, 2000, **404**, 746-748.
- 25 K. A. Dunphy Guzman, M. P. Finnegan and J. F. Banfield, *Environ. Sci. Technol.*, 2006, **40**, 7688-7693.
- 26 H. Ogihara, J. Xie, J. Okagaki and T. Saji, *Langmuir*, 2012, **28**, 4605-4608.
- 27 M. I. Dafinone, G. Feng, T. Brugarolas, K. E. Tetley and D. Lee, *ACS Nano*, 2011, **5**, 5078-5087.
- 28 X. Deng, L. Mammen, H. J. Butt and D. Vollmer, *Science*, 2012, **335**, 67-70.
- 29 L. Feng, Y. Zhang, J. Xi, Y. Zhu, N. Wang, F. Xia and L. Jiang, *Langmuir*, 2008, **24**, 4114-4119.
- 30 G. McHale, *Langmuir*, 2009, **25**, 7185-7187.
- 31 B. Bhushan and M. Nosonovsky, *Philos. Trans. Royal Soc. A*, 2010, **368**, 4713-4728.
- 32 O. I. Vinogradova, *Int. J. Miner. Process.*, 1999, **56**, 31-60.
- 33 C. Sendner, D. Horinek, L. Bocquet and R. R. Netz, *Langmuir*, 2009, **25**, 10768-10781.
- 34 H. Y. Erbil, A. L. Demirel, Y. Avci and O. Mert, *Science*, 2003, **299**, 1377-1380.
- 35 A. Lafuma and D. Quéré, *Nat. Mater.*, 2003, **2**, 457-460.
- 36 Q. Fu, X. Wu, D. Kumar, J. W. Ho, P. D. Kanhere, N. Srikanth, E. Liu, P. Wilson and Z. Chen, *ACS Appl. Mater. Interfaces*, 2014, **6**, 20685-20692.
- 37 Y. Shen, J. Tao, H. Tao, S. Chen, L. Pan and T. Wang, *Langmuir*, 2015, **31**, 10799-10806.
- 38 J. Amalvy, M. Percy, S. Armes and H. Wiese, *Langmuir*, 2001, **17**, 4770-4778.
- 39 P. Kim, T. S. Wong, J. Alvarenga, M. J. Kreder, W. E. Adorno-Martinez and J. Aizenberg, *ACS Nano*, 2012, **6**, 6569-6577.
- 40 E. Rio, A. Daerr, B. Andreotti and L. Limat, *Phys. Rev. Lett.*, 2005, **94**, 024503.
- 41 L. Gao and T. J. McCarthy, *Langmuir*, 2006, **22**, 6234-6237.
- 42 S. Suzuki, A. Nakajima, N. Yoshida, M. Sakai, A. Hashimoto, Y. Kameshima and K. Okada, *Chem. Phys. Lett.*, 2007, **445**, 37-41.
- 43 S. Jung, M. Dorrestijn, D. Raps, A. Das, C. M. Megaridis and D. Poulikakos, *Langmuir*, 2011, **27**, 3059-3066.
- 44 F. Tavakoli, S. H. Davis and H. P. Kavehpour, *J. Coat. Technol. Res*, 2015, **12**, 869-875.
- 45 Q. T. Fu, E. J. Liu, P. Wilson and Z. Chen, *Phys. Chem. Chem. Phys.*, 2015, **17**, 21492-21500.
- 46 H. Sojoudi, G. H. McKinley and K. K. Gleason, *Mater. Horizons*, 2015, **2**, 91-99.
- 47 L. Mazzola, *Surf. Eng.*, 2016, **32**, 733-744.
- 48 S. Kimura, Y. Yamagishi, A. Sakabe, T. Adachi and M. Shimanuki, *A new surface coating for prevention of icing on airfoils*, Report 0148-7191, SAE Technical Paper, 2007.
- 49 Y. Huang, M. Hu, S. Yi, X. Liu, H. Li, C. Huang, Y. Luo and Y. Li, *Thin Solid Films*, 2012, **520**, 5644-5651.
- 50 G. Tang, Y. H. Yeong and M. Khudiakov, *Advances in Polymer Science*, Springer, Berlin, Germany, 2017, 1-17.
- 51 R. Menini and M. Farzaneh, *Surf. Coat. Technol.*, 2009, **203**, 1941-1946.
- 52 R. Menini, Z. Ghalmi and M. Farzaneh, *Cold Reg. Sci. Technol.*, 2011, **65**, 65-69.
- 53 G. Momen and M. Farzaneh, *Appl. Surf. Sci.*, 2014, **299**, 41-46.
- 54 M. Esfandeh, S. Mirabedini, S. Pazokifard and M. Tari, *Colloids Surf. Physicochem. Eng. Aspects*, 2007, **302**, 11-16.
- 55 J. Gao, A. Martin, J. Yatvin, E. White and J. Locklin, *J. Mater. Chem. A*, 2016, **4**, 11719-11728.
- 56 N. Wang, D. Xiong, Y. Deng, Y. Shi and K. Wang, *ACS Appl. Mater. Interfaces*, 2015, **7**, 6260-6272.
- 57 R. Liao, Z. Zuo, C. Guo, Y. Yuan and A. Zhuang, *Appl. Surf. Sci.*, 2014, **317**, 701-709.
- 58 D. K. Owens and R. Wendt, *J. Appl. Polym. Sci.*, 1969, **13**, 1741-1747.
- 59 D. Kaelble, *J. Adhes.*, 1970, **2**, 66-81.
- 60 W. Rabel, *Farbe und Lack*, 1971, **77**, 997-1006.